

ARTICLE OPEN



Stress-assisted corrosion behaviour of Hastelloy N in FLiNaK molten salt environment

Yufen Gu¹, Wenzhu Zhang¹, Youwei Xu¹ , Yu Shi¹  and Korzhyk Volodymyr²

The use of molten-salt-based energy production and storage systems requires high-temperature corrosion- and creep-resistant structural materials. This study investigated the microstructure evolution and corrosion characteristics of Hastelloy N under working stress in a molten salt environment. Selective diffusion of Cr at the grain boundaries (GBs) of the Hastelloy N degraded the properties of the GBs, making them preferred locations for corrosion crack invasion. Stress further promoted Cr diffusion and accelerated GB carbide precipitation, thereby forming a corrosion couple between the carbide and matrix that facilitated the expansion of intergranular corrosion cracks into the grains. These findings are useful for providing advances in the design of novel structural alloys with extraordinary property-microstructure stability combinations for resistant to complex molten salt environments.

npj Materials Degradation (2022)6:90; <https://doi.org/10.1038/s41529-022-00300-x>

INTRODUCTION

Compared with conventional heat transfer fluids, molten salt exhibits excellent thermal conductivity, a large specific heat capacity, and relatively low viscosity¹. Consequently, molten salt has significant potential as an effective heat transfer and storage medium, which is necessary to support intermittent renewable energy generation^{2,3}. Therefore, molten salt has been widely explored as a heat transfer medium for next-generation low-emission power generation systems, such as concentrated solar power stations and molten salt reactors^{4,5}.

The accelerated development of molten-salt-based energy production and storage systems largely depends on the continuous development and testing of potential structural materials. Heat transfer based on molten salt requires structural materials with high-temperature corrosion and creep resistance^{6,7}. Therefore, the development and standardisation of structural materials that are resistant to molten salt is key for the application of molten salt as a heat transfer and storage medium. Oak Ridge National Laboratory (USA) and the Institute of Metal Research, Chinese Academy of Sciences (China) have developed alloy materials that are resistant to molten salt corrosion, such as Hastelloy N and GH3535 alloys, respectively. The corrosion properties of these alloys have been tested in high-temperature molten fluoride salt systems at 700 °C in air and inert environments^{8–10}; notably, the Hastelloy N and GH3535 alloys exhibited good molten salt corrosion resistance. Nevertheless, these materials cannot meet the corrosion rate requirements for commercial applications. Specifically, the annual average corrosion rate of molten-salt-resistant alloy materials in a high-temperature (700 °C) fluoride salt environment should be <25 μm¹¹.

The corrosion resistance of molten-salt-resistant structural materials depends on the material composition, molten salt composition, and molten salt purity. These factors reflect the thermodynamic driving force of the alloy elements dissolving into molten salt and diffusion rate of the alloy elements from the matrix to the surface^{12–14}. Because the operating temperature of

molten salt is significantly higher than that of a conventional heat transfer medium, alloy materials under the action of molten salt experience performance-limiting conditions, whereby small environment fluctuations lead to significant changes in the material structure and properties^{15,16}.

Determination of the corrosion behaviour of metals under a service load is essential in evaluating their service life. Stress corrosion is the most common form of failure for austenitic alloys subjected to high temperatures and pressures in a corrosive medium^{17–19}. In practical applications, nuclear power components operate under a load lower than their yield strength. However, the residual stress caused by welding, as well as thermal expansion and contraction caused by power changes due to nuclear power peak shaving, produces a large axial load on the heat exchange pipeline, triggering local plastic deformation. The areas experiencing plastic deformation become critical points in determining the service life of the components^{20–22}. Plastic slip increases the activation energy of a metal matrix, thereby increasing the rate of corrosion. Moreover, the accumulation of crystal defects at the grain boundaries (GBs) during slip deformation weakens the properties of GBs^{23,24}. Under the action of stress, nanoprecipitation occurs at the GBs, which often leads to their reduced cohesion strength²⁵.

Previously, high-temperature creep and no-load molten salt immersion tests were employed to study the service reliability of molten-salt-resistant structural materials in a simulated molten salt environment. The creep characteristics of molten-salt-resistant structural materials were studied under different loading conditions to reveal the effects of different molten salt systems and molten salt impurities on corrosion resistance. The nucleation and propagation of creep cracks were found to be closely related to the precipitation of intergranular carbides at the temperature of the molten salt service condition^{15,26,27}. Moreover, the scale and distribution of intergranular precipitates were important factors in determining the corrosion characteristics of molten-salt-resistant structural materials^{28,29}. Therefore, in an evaluation system, it is important to consider the influence of the service load on the

¹State Key Laboratory of Advanced Processing and Recycling of Non-ferrous Metals, Lanzhou University of Technology, Lanzhou, PR China. ²Zhejiang E.O. Paton Welding Technology Institute, Hangzhou, PR China. ✉email: xuyouwei_lut@163.com; shiyu@edu.lut.cn

corrosion-related structural integrity and service life of molten-salt-resistant structural materials.

Therefore, to accurately characterise and explore the stress-assisted corrosion behaviour of Hastelloy N in a molten salt system, it is important to understand the failure behaviour of Hastelloy N in a simulated molten salt environment and effectively evaluate its service life. In this study, the evolution of the corrosion film based on different mechanical and chemical properties of the material and molten salt system was also considered. The effect of stress on the selective diffusion of alloy elements with GB-dominant diffusion was analysed. Thus, the results of this study are significant for the safety, maintenance, and economic feasibility of molten salt systems.

RESULTS

Hastelloy N microstructure

The microstructure of the hot-rolled Hastelloy N (UNS N10003) is shown in Fig. 1. Its composition is 17.2 wt% Mo, 6.95 wt% Cr, 4.06 wt% Fe, 0.63 wt% Mn, 0.054 wt% C, 0.43 wt% Si, 0.03 wt% Al, and the remainder is Ni. The Hastelloy N has austenite grains with several annealing twins. Further, a large number of primary precipitates, which have been identified as M_6C carbides (where M is an alloy element, such as Ni, Mo, Cr, or Fe)³⁰, are distributed in the grains of the Hastelloy N.

Corrosion weight loss and morphology

The weight losses of the unloaded and loaded Hastelloy N samples immersed in FLiNaK salts at 700 °C for 240 h were 1.31 ± 0.15 and 5.18 ± 0.97 mg/cm², respectively. After applying stress, the weight loss of the samples significantly increased up to four times that of the unloaded samples. Supplementary Fig. 1 shows the weight loss rate of the Hastelloy N obtained in this study and those of Hastelloy N and GH3535 alloys reported in the literature in a FLiNaK molten salt environment and a FLiNaK

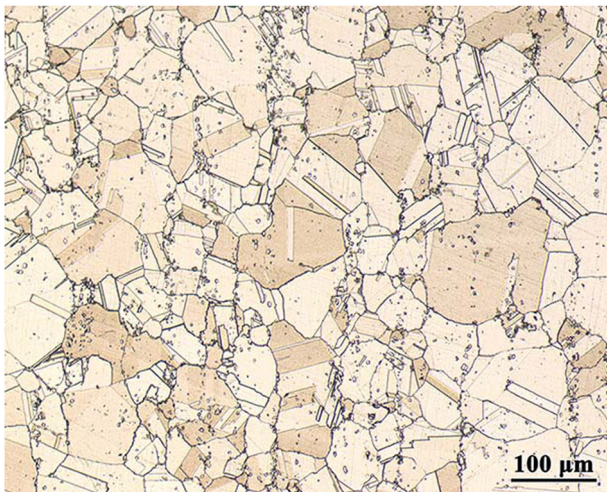


Fig. 1 Microstructure of Hastelloy N.

molten salt environment with impurities. In the temperature range of 650–750 °C, previous studies reported a weight loss rate of approximately 0.0006–0.0093 mg/cm² h for Hastelloy N and GH3535 alloys in the molten salt environment, which is similar to the weight loss rate of the unloaded sample in this study. However, the application of stress significantly increased the weight loss rate to 0.022 mg/cm² h. Therefore, stress is determined to be the main factor that affects the weight loss rate of Hastelloy N in a molten salt environment.

The Ni, Mo, Mn, Cr, and Fe contents in the FLiNaK salt before and after the corrosion test were determined by inductively coupled plasma optical emission spectrometry (ICP-OES), as shown in Table 1. After corrosion, the Mo, Cr, and Ni contents in the molten salt increased, whereas the Fe decreased, regardless of the stress condition. In addition, the changes in the metal ion contents in the molten salt after corrosion of the loaded samples were significantly greater than those of the unloaded samples.

Corrosion on the surface was investigated by scanning electron microscopy (SEM). The surface corrosion morphology of the Hastelloy N after immersion in a molten salt environment for 240 h under unloaded and loaded conditions is shown in Fig. 2. The sample surface exhibits a uniform and porous corrosion film in the unloaded state. In contrast, in the loaded state, the surface of the corrosion film exhibits ridge protrusions. The size of the area surrounded by the ridge protrusion is approximately 70–100 μm, which is similar to the grain size of the Hastelloy N. Therefore, the Hastelloy N experienced notable intergranular corrosion (IGC) at an accelerated rate with stress application. The faster IGC rate produced a large amount of corrosion products that accumulated along the GBs, resulting in their ridge shape.

The corrosion morphology of the cross-section of the Hastelloy N after immersion in a molten salt environment for 240 h under unloaded and loaded conditions is shown in Fig. 3. The area near the surface of the sample affected by the molten salt corrosion exhibits a white colour, which is in sharp contrast to the base metal. This white area is usually called the ‘white etching zone’, which is regarded as the area affected by the corrosive medium on the sample surface during corrosion³¹. In the unloaded state, the Hastelloy N also exhibited distinct IGC characteristics, reaching an IGC crack length of up to 100 μm, which was not reflected on the surface corrosion morphology. The molten salt erosion area was limited to the location of the GBs. A change in the direction of the GBs did not effectively prevent IGC cracks from extending along the GBs to the interior of the matrix. When stress was applied, IGC intensified, as indicated by the serious erosion of the grains on the sample surface and increased IGC crack length spanning two to three grains. Furthermore, the IGC cracks extended to both sides of the GBs, suggesting IGC expansion into the grains. Therefore, the stress-assisted corrosion of the Hastelloy N in a molten salt environment was mainly demonstrated by the transverse extension of the corrosion area from the GBs to the grain interior, rather than the unrestricted longitudinal extension to the interior of the alloy.

To analyse the elemental distribution of Hastelloy N under different loading conditions, the elemental distribution at the interface of the white etching zone on the cross-section of corrosion samples was tested by electron probe microanalysis

Table 1. Chemical compositions of FLiNaK salts before and after corrosion tests.

	Ni (ppm by weight)	Mo (ppm by weight)	Cr (ppm by weight)	Fe (ppm by weight)
As-received FLiNaK	5.78 ± 0.08	6.80 ± 0.02	30.50 ± 0.01	165.23 ± 0.02
FLiNaK (unloaded)	6.38 ± 0.09	55.53 ± 0.23	37.82 ± 0.16	146.89 ± 0.19
FLiNaK (loaded)	8.12 ± 0.01	144.00 ± 1.82	49.87 ± 0.95	98.73 ± 0.82

Note: Each value is the averaged of three data points, reported as mean \pm standard deviation.

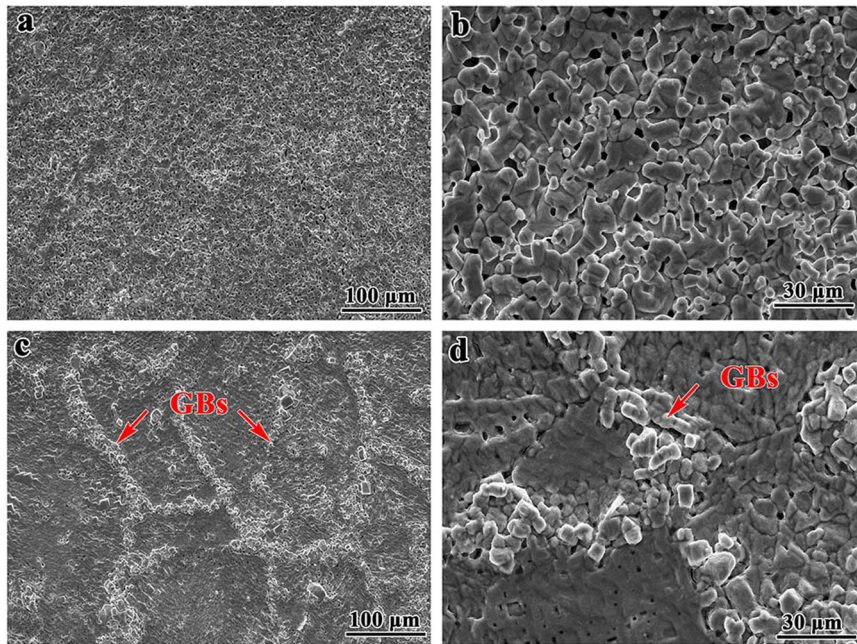


Fig. 2 SEM images of the surface morphology of the Hastelloy N after corrosion in a molten salt environment for 240 h. **a, b** unloaded, **c, d** loaded.

(EPMA). Figure 4 shows the elemental distribution of the unloaded samples. C exhibited granular agglomeration, which was attributed to the carbide formed at the GBs. In addition, the GBs were Cr- and Ni-deficient with slightly abundant Mo. The disintegration of the major alloying elements resulted in GB cavitation, which is the primary cause of creep and corrosion failure in superalloys³².

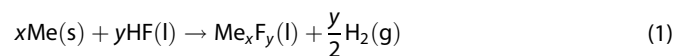
Figure 5 shows the elemental distribution of the loaded samples. An evident desolvation zone was noted near the surface of the sample in the crystal and at the GBs. In addition, the C content near the desolvation zone was accumulated densely and distributed in the chains along the GBs. The degree of C segregation increased significantly after stress application. The GBs below the desolvation zone boundary have a low Cr content, whereas those above the desolvation zone boundary have a high Cr content. This result is attributed to the role of GBs as the main channel for element diffusion, whereby alloy elements below the boundary of the desolvation zone diffuse along the GBs, resulting in their lower content below the desolvation zone. In addition, this element distribution is related to the difference in the stress distribution, which will be discussed later. The Ni-poor area at the GBs was the same as that without stress, but was notably wider than that without stress. The distribution of Mo was opposite to that of Cr. The GBs below the boundary of the desolvation zone were rich in Mo, whereas those above the boundary were poor in Mo. The dissolution of Mo at the GBs in the desolvation zone is likely to cause the significant increase of Mo content in the molten salt corrosion medium after the corrosion test (Table 1).

Corrosion product characterisation

The X-ray diffractometry (XRD) patterns of the as-received sample and unloaded and loaded samples after corrosion are shown in Fig. 6. The XRD patterns revealed that the corrosion products formed on the sample surface after corrosion were mainly composite fluorides such as Na_3FeF_6 and KNa_3CrF_6 . This is attributed to the fluorides MF_2 and MF_3 produced in the corrosion reaction, which acted as Lewis acids and interacted with the Lewis base F^- (LiF/NaF/KF) to form complexes such as $[\text{MF}_4]^{2-}$, $[\text{MF}_4]^-$, and $[\text{MF}_6]^{3-}$ ³³. Thereafter, $[\text{MF}_6]^{3-}$ and K^+/Na^+ reacted to form $\text{K}_3\text{FeF}_6/\text{K}_2\text{Na}_3\text{CrF}_6$ complexes, which were deposited on the

surface of the samples and in the GBs. In addition, after high-temperature corrosion, the Hastelloy N formed M_6C carbides. The peak amplitudes of Na_3FeF_6 , KNa_3CrF_6 , and M_6C increased significantly when stress was applied, indicating that the application of stress significantly promoted the corrosion rate of Hastelloy N in molten salt.

To analyse the mechanism of element dissolution at the GBs of Hastelloy N in FLiNaK molten salt, transmission electron microscopy (TEM) samples were prepared at the GBs of the loaded samples after corrosion using focused ion beam (FIB) milling. The element distribution was also characterised by TEM-energy-dispersive X-ray spectroscopy (EDS), as shown in Fig. 7. The corrosion products at the GBs were rich in Cr (Fig. 7d) and Mo (Fig. 7g), whereas the interface between the corrosion products and matrix was rich in Fe (Fig. 7c) and Ni (Fig. 7f). Both TEM-EDS and EPMA results confirmed that Cr was the element with the highest tendency to diffuse along the GBs during immersion corrosion of the Hastelloy N in the FLiNaK molten salt environment. This was related to the standard Gibbs free energy of the main elements of the Hastelloy N involved in producing fluoride corrosion products. Corrosion in molten salt is an impurity-driven process^{34–36}, and typical impurities include H_2O and SO_4^{2-} . The impurities in the salt provide pathways for corrosion by forming relatively unstable fluorides, such as HF, which tend to corrode the alloy materials by a reaction such as



The Gibbs free energy of fluorinated salts formed by the main alloy elements of Hastelloy N through Eq. (1) at 700 °C was calculated and shown in Supplementary Table 1.

The condition for equilibrium of Eq. (1) is given by³⁷

$$\Delta G_{700^\circ\text{C}}^0 = -RT \ln \frac{a_{\text{Me}_x\text{F}_y} a_{\text{H}_2}^{y/2}}{a_{\text{Me}}^x a_{\text{HF}}^y} \quad (2)$$

here, a_i is the chemical activity of the i th component, respectively. For ease of calculation, we assume that the oxides are pure and immiscible such that $a_{\text{Me}_x\text{F}_y} = 1$. These calculations showed that under the same corrosion conditions, the chemical activity of Cr at

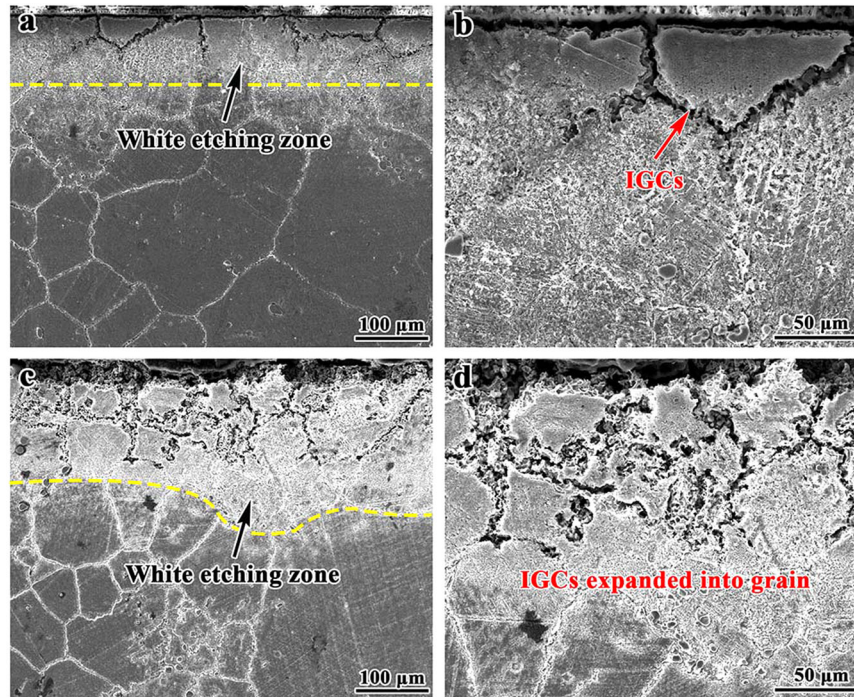
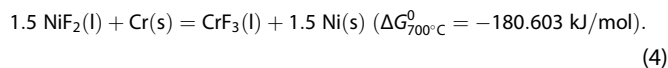
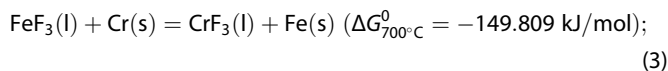


Fig. 3 SEM images of the cross-section morphology of the Hastelloy N after corrosion in a molten salt environment for 240 h. a, b unloaded, and c, d loaded.

the corrosion interface is at least ten orders of magnitude higher than that of other alloy elements. Therefore, compared with Fe, Ni, and Mo, the concentration of Cr required to maintain the equilibrium of Eq. (2) is extremely small. Therefore, after the corrosion reaction occurs, the concentration of Cr at the corrosion interface will be much smaller than that of other alloy elements, and the corresponding concentration gradient of Cr is much larger. The diffusion tendency of Cr along the gradient direction is thus higher. In addition, FeF_3 and NiF_2 in the corrosion products of Hastelloy N will promote the dissolution of Cr through Eqs. (3) and (4)^{38,39}. This can explain the high proportion of Fe and Ni at the interface between the corrosion products and the matrix in Fig. 7c, f, even though the content of Fe and Ni in the molten salt decreased after the immersion test (Table 1).



GB carbide characterisation

The evolution characteristics of the precipitated phase of the alloy are important for its corrosion resistance reliability under high-temperature service environments. The characteristics of the GB carbide in the as-received, unloaded, and loaded samples of the Hastelloy N after thermal exposure are shown in supplementary Fig. 2. There were only a small number of precipitates at the GBs on the substrate before thermal exposure. After 240 h of heat exposure, the distribution of the precipitates on the GBs changed from intermittent point distribution to intermittent sheet distribution. In addition, the size and quantity of the precipitates significantly increased. After stress loading and heat exposure for 240 h, the size of the precipitates further increased, and they became connected along the GBs. According to the XRD results (Fig. 6) and previous reports^{40,41}, the carbide precipitated at the

GBs of the Hastelloy N under the 700 °C service state was determined to be M_6C . The EPMA results of the carbides precipitated at the GBs are shown in Supplementary Table 2. The Mo and Cr contents in the GB carbides of the as-received and loaded samples were relatively high after thermal exposure, even with Ni as the dominant element in the Hastelloy N.

To analyse the effects of carbide precipitated at GBs on the corrosion properties of Hastelloy N, the potential distribution at the GBs was analysed by atomic force microscopy (AFM). Figure 8 shows the topographic map and voltage potential map near the GBs of the heat-exposed loaded Hastelloy N sample. The topographic map of the polished sample shows the protrusion corresponding to the GBs, which is hundreds of nanometres higher than the matrix on both sides owing to the high hardness of GB carbides. In addition, the Volta-potential in the GB region was significantly higher than that in the matrix on both sides. The potential difference reached 150 mV at 50 μm . The relatively high potential was attributed to the chain carbides precipitated in the GB region, which led to the dissolution of the noble metals near the GB region. The AFM results showed that a significant corrosion couple was formed between the carbides near the GBs and the substrate on both sides of the electrolyte. Specifically, the carbides acted as the cathode and the substrate on both sides acted as the anode, which resulted in the area near the GBs having the highest vulnerability to corrosion. This observation was consistent with the results of the molten salt immersion corrosion morphology in Fig. 3c, d. In addition, in the molten salt immersion corrosion test, the IGC cracks expanded into the grains after stress was applied, which can also be related to the strong galvanic corrosion near the GBs caused by the precipitation of large carbide network at the GBs, resulting in the continuous dissolution of the metal matrix on both sides of the carbide.

DISCUSSION

Because different grains on the GBs have different particle arrangements and orientations, the GB structure has a more pronounced surface effect than the grain density. In addition, the

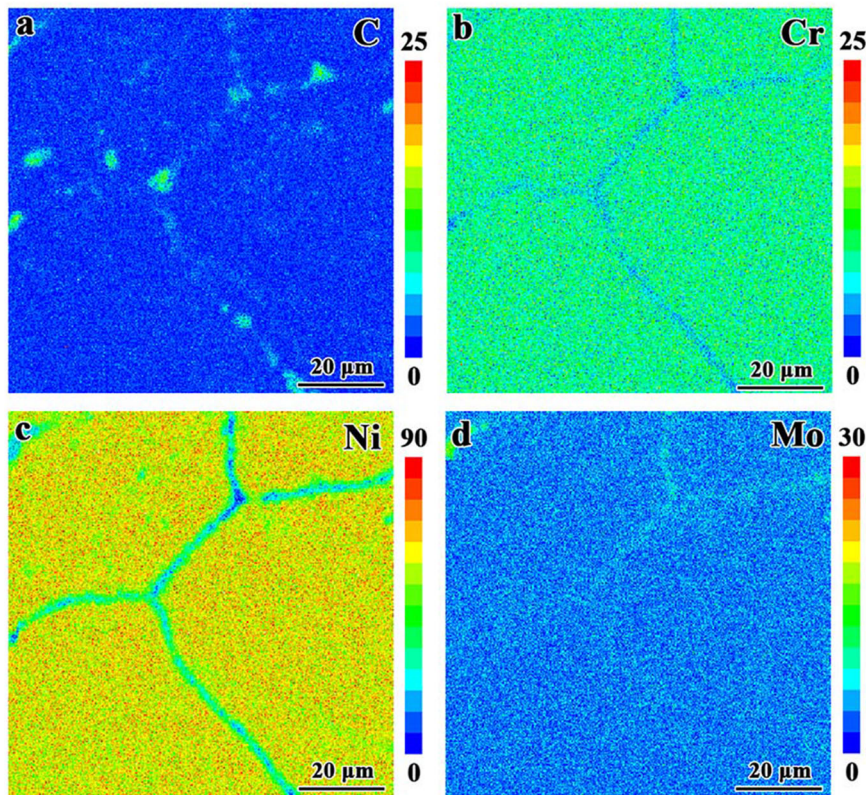


Fig. 4 EPMA results of the elemental distribution near the white etching zone of the unloaded Hastelloy N after 240 h in molten salt. **a** C, **b** Cr, **c** Ni, and **d** Mo.

energy of the solute atoms in the grain is higher than that at the GBs, resulting in the spontaneous gravitation of the solute atoms toward the GBs. The calculation of the Gibbs free energy of the carbides formed by the main elements in the Hastelloy N alloy at 700 °C yielded a positive Gibbs free energy for the Ni and Fe carbides, whereas that of the Cr and Mo carbides was negative⁴². Hence, the formation of Ni₃C and Fe₃C is unfavourable, whereas that of Mo₃C and Cr₃C is favourable and stable. Therefore, the GB carbides observed in supplementary Fig. 2 are more likely to be Mo₃C and Cr₃C (Supplementary Table 2). The GB precipitates have an adverse effect on the plasticity and fracture strain of the Ni-based alloy under loading owing to the weak interface between the carbide and matrix, which may cause damage during loading⁴³. Particularly, triple GB precipitation, which results in stress concentration, generates the main failure area in the creep process. Under stress application, GB sliding produces holes or wedge cracks^{44,45}. In addition, carbide precipitation consumes carbon in the adjacent matrix, resulting in the softening of the adjacent material⁴⁶.

Ni-based alloys can withstand extreme service conditions with the addition of alloy elements Mo and Cr, which imparts the necessary high-temperature stability and corrosion resistance of the alloy in different media^{47,48}. Cr is a basic element of stainless steel and Ni-based alloys that aids in maintaining corrosion resistance. Particularly, the combination of Cr and O₂ can produce a corrosion-resistant Cr₂O₃ film. In addition, an increase in Cr content can improve the reparability of a passive film of steel. Hastelloy N is solution-strengthened with 16 wt% Mo, which stabilises the Ni₂Mo₄(C,Si) and Ni₃Mo₃(C,Si) primary precipitates in the alloys^{45,49}, and exhibits excellent creep resistance. In addition, colossal supersaturation with C continuously induces the diffusion of Cr and Mo to the GBs owing to their high carbon affinity⁴², thereby resulting in the easy formation of carbides without saturation.

The Gibbs free energies of the molten salt constituents (LiF, NaF, and KF) are more negative than those of the metallic fluorides in pure FLiNaK molten salt⁵⁰. Owing to the high affinity between Cr, molten salt, and molten salt impurities, Cr continues to diffuse along the GBs to the matrix surface. For example, the diffusion coefficient of Cr along the GBs is at least one order of magnitude higher than that in the grains: $D_{Cr,Grain} < 1E-13 \text{ cm}^2/\text{s} < D_{Cr,GB}$ ⁵¹. Accordingly, the outward diffusion of the alloying elements leads to GB cavitation, thereby diffusing molten salt and molten salt impurities inward along the GBs and accelerating the corrosion dissolution of the GBs. However, although Mo has a notable affinity for C, the Gibbs free energy of generating MoF₃, calculated by Eq. (1), is more positive than that of generating CrF₃, which implies the lower tendency of Mo to diffuse toward the GBs and react with molten salt impurities to form MoF₂. This makes it difficult for Mo to dissolve into the molten salt and diffuse along the GBs to the substrate surface, resulting in the observed abundance of Mo in the GBs (Figs. 4d and 5d). However, we still detected a significant increase in the Mo content by ICP-OES of the molten salt after the immersion corrosion test of the loaded sample (Table 1). This can be attributed to Mo₆C melting into the molten salt during the expansion of the IGC into the grain.

Therefore, from the above analysis, we determined that carbide precipitation and selective dissolution of the impurity elements lead to Cr loss in the GB region of Hastelloy N. Further, these are the main factors for the formation of IGC cracks in Hastelloy N in a molten salt environment.

In Ni-based alloys, carbides often precipitate and/or coarsen at the GBs under high temperatures and stresses. GB carbide coarsening rates have been reported to be three orders of magnitude greater than the stress or strain rates in creep tests^{52,53}. The tensile stress of solid materials can be relieved by dislocation slip movement, dislocation creep, diffusion flow, or cracks perpendicular to the direction of tensile stress. When the molten

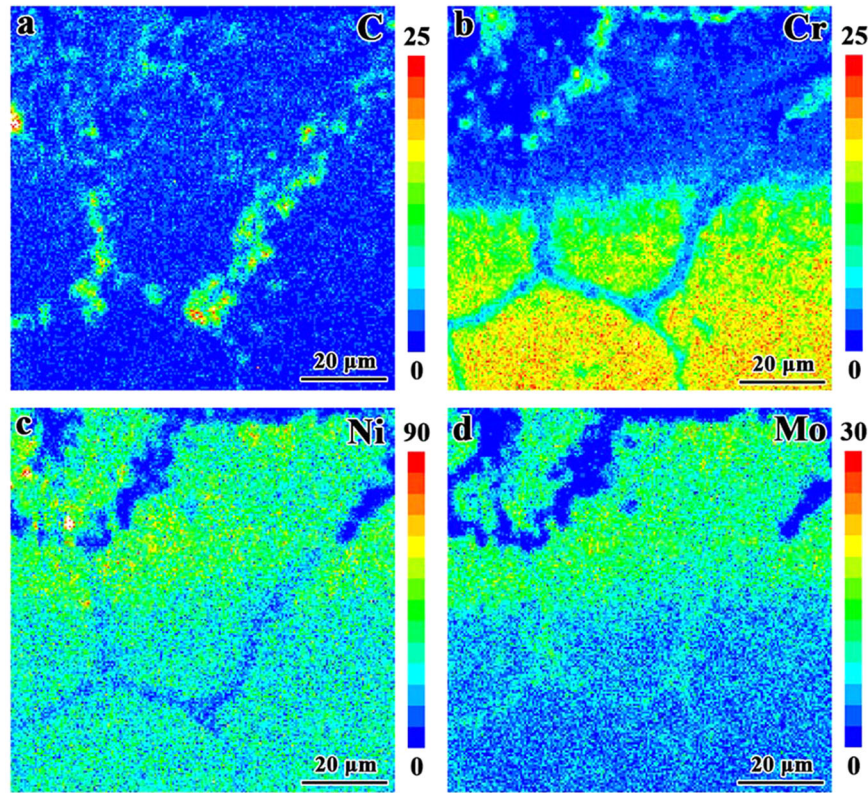


Fig. 5 EPMA results of the elemental distribution near the white etching zone of the loaded Hastelloy N after 240 h in molten salt. **a** C, **b** Cr, **c** Ni, and **d** Mo.

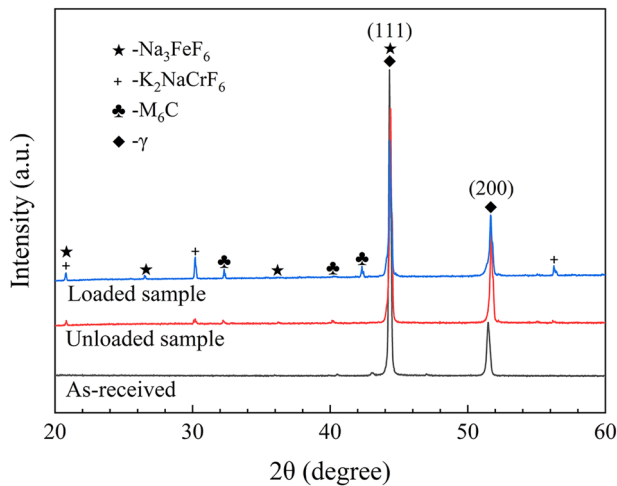


Fig. 6 Comparison of the XRD patterns of the Hastelloy N as-received sample, unloaded sample after corrosion, and loaded sample after corrosion.

salt test temperature exceeds $0.5T_m$ (T_m represents the melting point of the alloy), dislocation creep and vacancy flow have important effects on the diffusion of the alloy elements. The loading stress can trigger the dislocation-assisted alloying element migration mechanism and is also closely related to the alloying element flux. When the crystal is subjected to tensile stress, the dislocation and vacancy concentrations will be higher than those in the thermal equilibrium state. In contrast, under compressive stress, the dislocation and vacancy concentrations will be lower than those in the thermal equilibrium state.

According to the Nabarro–Herring creep model, under thermal equilibrium, the concentration of vacancies, C , in the tensile region is⁵⁴

$$C = C_0 \exp\left(\frac{\sigma a^3}{kT}\right), \quad (5)$$

where σa^3 is the work done by the stress for removing an atom, C_0 is the thermal equilibrium concentration of the vacancies in the stress-free region, T is the temperature in K, and k is the Boltzmann constant. In other words, after stress is applied, the vacancy concentration in the matrix significantly increases. Accordingly, a greater probability of element diffusion can be achieved through vacancy migration and diffusion.

The vacancy concentration gradient is given by⁵⁴

$$\frac{dC}{dx} = \frac{C_0}{L} \left[\exp\left(\frac{\sigma a^3}{kT}\right) - 1 \right], \quad (6)$$

where L is the distance between the stress and stress-free zones.

The diffusion flow of the alloying elements per unit time is

$$J_v = D_v \frac{dC}{dx}, \quad (7)$$

where D_v is the coefficient of surface diffusion of the alloying elements. Among the main elements of Hastelloy N, Cr has the highest affinity for F^- and second-highest affinity for $C^{42,55}$, resulting in the fastest rate of dissipation along the GBs, which is equivalent to the highest surface diffusion coefficient at the GBs. With the high mobility of the GBs, Cr has the maximum gradient between the GBs and interior of the matrix and the largest flux from the grains to the GBs. Therefore, stress has the most notable effect on the accelerated diffusion of Cr. Consequently, the rate of carbide formation on the GBs of Hastelloy N under stress increases, leading to a continuous network distribution (supplementary Fig. 2f). Moreover, during

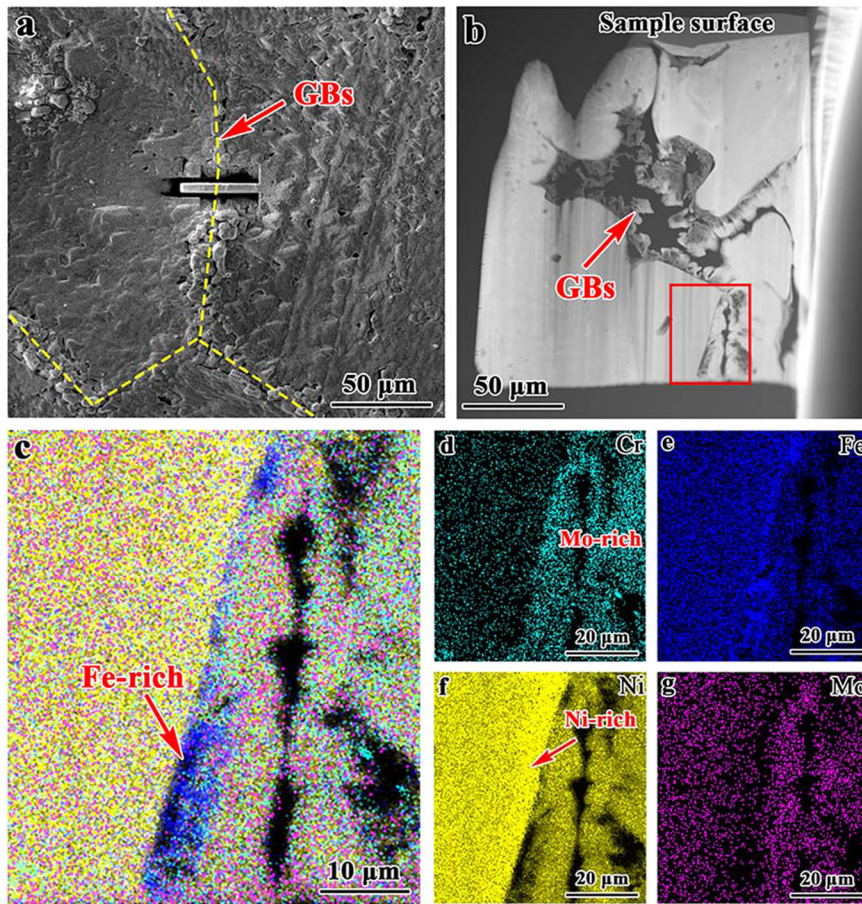


Fig. 7 TEM images of the corrosion products of Hastelloy N exposed to a FLiNaK molten salt environment. **a** FIB sampling position, **b** TEM sample (red rectangle indicates the sampling area), **c** TEM-EDS result of the corresponding region in **b**, and distribution of **d** Cr, **e** Fe, **f** Ni, and **g** Mo.

the stress-assisted immersion corrosion process, an increased amount of Cr diffuses into the molten salt through the GBs. Under the application of stress, the range of the GB degradation area is widened (Fig. 5); further, IGC cracks arise in this area and their width increases (Fig. 3d).

In addition, under all stress conditions, large carbides are formed, resulting in enhanced galvanic corrosion in the area near the carbides and accelerated corrosion of the matrix around the carbides. This results in the propagation of the IGC cracks into the grains, as well as the loosening of the carbides and their release from the alloy surface, resulting in an increase in the corrosion crack size (Fig. 3c, d). Accordingly, the scale of the diffusion channel of the elements to the substrate surface increases, further enhancing the corrosion rate of the entire substrate.

In summary, Hastelloy N exhibited a distinct IGC tendency in the FLiNaK molten salt environment. The GBs were the main channel of alloy element diffusion. Moreover, the diffusion of Cr along the GBs was the primary cause of IGC. Notably, the stress promoted Cr diffusion and accelerated the precipitation of grain boundary carbides, thereby forming a corrosion couple between the carbide and matrix, which promoted the expansion of intergranular corrosion cracks into the grains. Therefore, the development of alloys with substantial resistance to IGC expansion in complex molten salt service environments will be the focus of our future research.

METHODS

Materials

The microstructure of the hot-rolled Hastelloy N (UNS N10003) was examined by microscopy. Its composition was analysed by XRF. The molten salt used in this test was a FLiNaK ternary eutectic mixture (46.5 mol% LiF, 11.5 mol% NaF, and 42.0 mol% KF) provided by West Asia Chemical Technology Co., Ltd. (Shandong, China). The molten salt was of analytical grade.

Molten salt corrosion test

The material was cut into $130 \times 25 \times 5$ mm³ samples by wire cutting. Prior to the tests, the samples were ground using 2000-grit waterproof silicon carbide sandpaper, degreased with acetone, and cleaned with absolute ethanol. Subsequently, the samples were measured with Vernier callipers and weighed using an electronic balance with an accuracy of 0.1 mg.

A set of zirconia four-point bending fixtures was designed to apply stress to the sample according to ASTM G39-99 standard guidelines⁵⁶. The schematics of the fixture and assembly method are shown in Fig. 9. The inner side of the four-point bending specimen was subjected to compressive stress, whereas the outer side was subjected to tensile stress. In this study, only the corrosion behaviour of the outer side under tensile stress was investigated. The deflection of the specimens was monitored by a displacement meter; a maximum displacement of 1.5 mm was

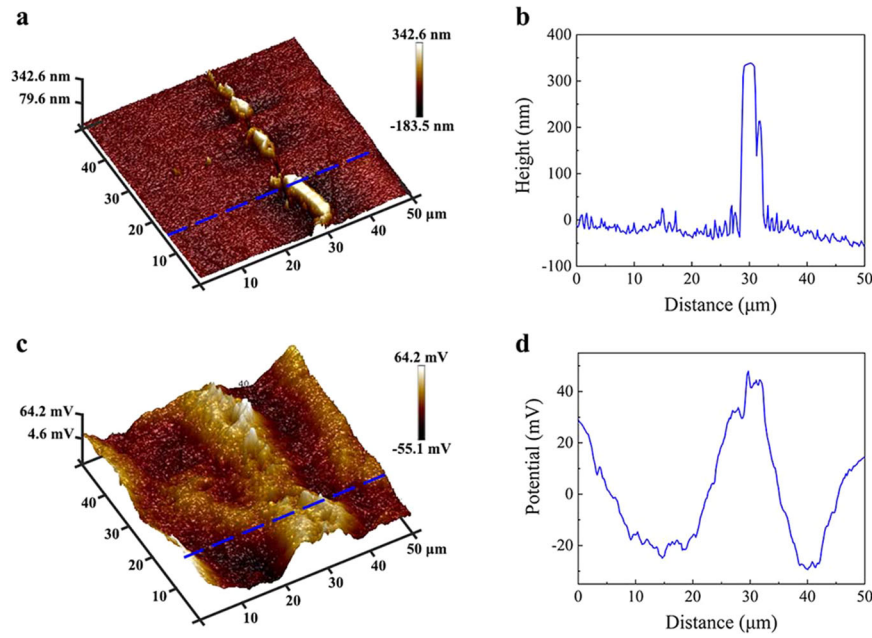


Fig. 8 AFM maps for the near-GB region of the heat-exposed loaded samples. **a** topographic map and **b** corresponding topographic profiles along the blue line in **a**; and **c** potential distribution and **d** corresponding Volta-potential profiles along the blue line in **c**.

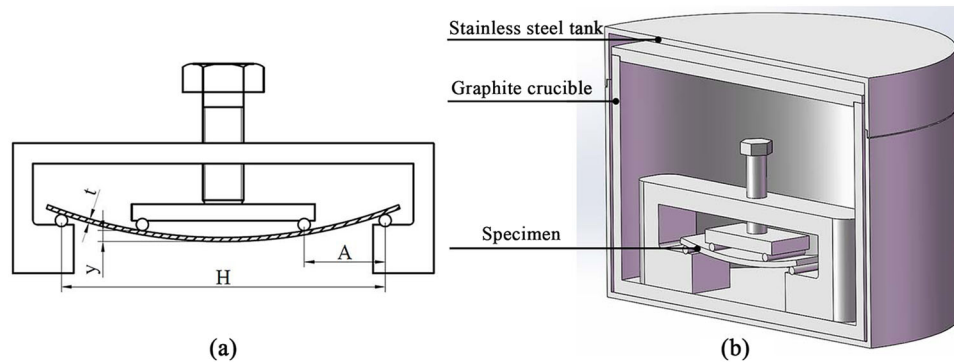


Fig. 9 Schematics of the fixture and assembly method. **a** the four-point bending fixture and **b** molten salt corrosion device.

noted. The maximum tensile stress σ was calculated as follows⁵⁶:

$$\sigma = \frac{12Et_y}{(3H^2 - 4A^2)}, \quad (8)$$

where E is the modulus of elasticity; t is the specimen thickness; y is the maximum deflection between the outer supports; H is the distance between the outer supports, which was set to 80 mm; and A is the distance between the outer and inner supports, which was set to 20 mm.

Before the tests, the 316 L stainless steel tank, zirconia fixture with assembled samples, and graphite crucible were cleaned with distilled water followed by alcohol, kept at 40 °C for 12 h in a vacuum drying oven, and transferred to a glove box filled with high-purity Ar (99.999%). In the glove box, the zirconia fixture with the assembled sample was fit into a graphite crucible. Thereafter, the graphite crucible was filled with 800 g of the FLiNaK salt ternary eutectic mixture, covered, and sealed inside the 316 L stainless steel tank. The sealed 316 L stainless steel tank with the complete assembly was transferred to a muffle furnace. It was heated and held at 700 °C for 240 h.

The tests were conducted in triplicate. In addition, samples assembled with the four-point bending fixture were tested in the

same molten salt corrosive environment without load for comparison. After the corrosion test, the 316 L stainless steel tank was cooled to room temperature in the muffle furnace, and the sample was removed from the molten salt. The sample was soaked in aqueous 1.0 M $\text{Al}(\text{NO}_3)_3$ solution for 24 h, and the residual FLiNaK salt was removed from the sample surface. Finally, after ultrasonic cleaning with alcohol, the sample was dried, weighed, and stored in a vacuum drying oven for subsequent sampling and characterisation. The chemistry of the salts after corrosion was analysed by ICP-OES (Thermo ICP 6300).

Experimental characterisation

According to the standard process of metallographic preparation, the samples were cut, ground, and mirror-polished. Subsequently, the samples were etched with a solution of 3 g $\text{CuSO}_4 + 10 \text{ mL H}_2\text{SO}_4 + 40 \text{ mL HCl} + 50 \text{ mL water}$ for 30 s. The microstructure of the samples was observed by optical microscopy (Zeiss Axio vert. A1). After the corrosion test, the morphology of the corrosion products and precipitates was observed by SEM (FEI Nanosem 430). EPMA (Shimadzu, EPMA-1600) was used to detect the distribution of the alloying

elements. An X-ray diffractometer (Bruker D8 Advance) with Cu-K α radiation (1.54 Å) was employed to measure the crystal phases of the samples before and after corrosion. In addition, corrosion film samples were prepared by FIB milling (Helios Nanolab 460HP) and examined using a transmission electron microscope (FEI–Tecnai G2 F30) equipped with selected-area electron diffraction and EDS. Topography and Volta potential images of the Hastelloy N in GBs were obtained using a commercial atomic force microscope (Bruker, Dimension Icon) with a Kelvin scanning probe. All AFM mappings were conducted on the mirror-polished metallographic sample surfaces.

DATA AVAILABILITY

The data that support this investigation are available from the corresponding author upon reasonable request.

Received: 10 May 2022; Accepted: 16 October 2022;

Published online: 10 November 2022

REFERENCES

- Han, Y., Zhang, C., Wu, Y. & Lu, Y. Investigation on thermal performance of quaternary nitrate-nitrite mixed salt and solar salt under thermal shock condition. *Renew. Energ.* **175**, 1041–1051 (2021).
- Guillot, S. et al. Corrosion effects between molten salts and thermal storage material for concentrated solar power plants. *Appl. Energ.* **94**, 174–181 (2012).
- González-Roubaud, E., Pérez-Osorio, D. & Prieto, C. Review of commercial thermal energy storage in concentrated solar power plants: steam vs. molten salts. *Renew. Sustain. Energy Rev.* **80**, 133–148 (2017).
- Mallapaty, S. China prepares to test thorium-fuelled nuclear reactor. *Nature* **597**, 311–312 (2021).
- Ding, W. & Bauer, T. Progress in research and development of molten chloride salt technology for next generation concentrated solar power plants. *Engineering* **7**, 334–347 (2021).
- Martinek, J., Jape, S. & Turchi, C. S. Evaluation of external tubular configurations for a high-temperature chloride molten salt solar receiver operating above 700 °C. *Sol. Energy* **222**, 115–128 (2021).
- Muránsky, O. et al. Impact of dislocations and dislocation substructures on molten salt corrosion of alloys under plasticity-imparting conditions. *Corros. Sci.* **176**, 108915 (2020).
- Yin, H. et al. Corrosion behavior and mechanism of GH3535 alloy in NaOH, HF and H₂O₂ solution. *J. Alloy. Compd.* **887**, 161387 (2021).
- Guo, S., Zhang, J., Wu, W. & Zhou, W. Corrosion in the molten fluoride and chloride salts and materials development for nuclear applications. *Prog. Mater. Sci.* **97**, 448–487 (2018).
- Ye, X. et al. The high-temperature corrosion of Hastelloy N alloy (UNS N10003) in molten fluoride salts analysed by STXM, XAS, XRD, SEM, EPMA, TEM/EDS. *Corros. Sci.* **106**, 249–259 (2016).
- Zhou, X. et al. Development strategy for thorium molten salt reactor materials. *Chin. J. Eng. Sci.* **21**, 29 (2019).
- Zhang, J. et al. Redox potential control in molten salt systems for corrosion mitigation. *Corros. Sci.* **144**, 44–53 (2018).
- Qiu, J. et al. Effect of SO₄²⁻ on the corrosion of 316L stainless steel in molten FLiNaK salt. *Corros. Sci.* **144**, 224–229 (2018).
- Xue, W. et al. Effects of silicon carbide on the corrosion of metallic materials in molten LiF-NaF-KF salt. *Corros. Sci.* **143**, 157–165 (2018).
- Fan, G., Wang, W., Shi, W., Wang, S. & Lu, Y. Creep crack growth of GH3535 alloy at elevated temperatures. *Mater. Charact.* **181**, 111412 (2021).
- González-Gómez, P. A., Rodríguez-Sánchez, M. R., Laporte-Azcué, M. & Santana, D. Calculating molten-salt central-receiver lifetime under creep-fatigue damage. *Sol. Energy* **213**, 180–197 (2021).
- Chang, L. et al. Effect of machining on stress corrosion crack initiation in warm-forged type 304L stainless steel in high temperature water. *Acta Mater.* **165**, 203–214 (2019).
- Kuang, W., Song, M. & Was, G. S. Insights into the stress corrosion cracking of solution annealed alloy 690 in simulated pressurized water reactor primary water under dynamic straining. *Acta Mater.* **151**, 321–333 (2018).
- Meisnar, M., Vilalta-Clemente, A., Moody, M., Arioka, K. & Lozano-Perez, S. A mechanistic study of the temperature dependence of the stress corrosion crack growth rate in SUS316 stainless steels exposed to PWR primary water. *Acta Mater.* **114**, 15–24 (2016).
- Xu, Y., Jing, H., Xu, L., Han, Y. & Zhao, L. Effect of overload on the oxidation behavior of CF8A austenitic stainless steel in a high-temperature water environment. *Corros. Sci.* **162**, 108219 (2020).
- Ahn, T. M. Long-term initiation time for stress-corrosion cracking of alloy 600 with implications in stainless steel: review and analysis for nuclear application. *Prog. Nucl. Energ.* **137**, 103760 (2021).
- Maric, M. et al. The effect of cold-rolling on the microstructure and corrosion behaviour of 316L alloy in FLiNaK molten salt. *Corros. Sci.* **142**, 133–144 (2018).
- Stratulat, A., Duff, J. A. & Marrow, T. J. Grain boundary structure and intergranular stress corrosion crack initiation in high temperature water of a thermally sensitised austenitic stainless steel, observed in situ. *Corros. Sci.* **85**, 428–435 (2014).
- Xu, Y., Jing, H., Xu, L., Han, Y. & Zhao, L. Microstructural evolution and oxidation behaviour of CF8A austenitic stainless steel during corrosion fatigue in a simulated pressurised water reactor environment. *Corros. Sci.* **163**, 108286 (2020).
- Liu, Z., Hou, Q., Li, C., Li, X. & Shao, J. Correlation between grain boundaries, carbides and stress corrosion cracking of Alloy 690TT in a high temperature caustic solution with lead. *Corros. Sci.* **144**, 97–106 (2018).
- Spader, D., Lapera, M. & Ghonem, H. A coupled, physics-based matrix-grain boundary model for creep of carbide strengthened nickel-based superalloys - II. *Mater. Sci. Eng.: A* **769**, 138355 (2020).
- Han, F. F. et al. Effect of long-term thermal exposure on the hot ductility behavior of GH3535 alloy. *Mater. Sci. Eng.: A* **673**, 299–306 (2016).
- Li, X. et al. Effect of thermal aging on corrosion behavior of type 316H stainless steel in molten chloride salt. *Corros. Sci.* **191**, 109784 (2021).
- Xu, H. et al. Non-uniform corrosion of UNS N10003 alloy induced by trace SO₄²⁻ in molten FLiNaK salt. *Corros. Sci.* **192**, 109802 (2021).
- Muránsky, O. et al. Molten salt corrosion of Ni-Mo-Cr candidate structural materials for Molten Salt Reactor (MSR) systems. *Corros. Sci.* **159**, 108087 (2019).
- Buntain, R., Alexandrov, B. & Viswanathan, G. Characterization of the interpass microstructure in low alloy steel/Alloy 625 HW-GTAW narrow groove welds. *Mater. Charact.* **170**, 110638 (2020).
- Wen, J. et al. Environmentally enhanced creep crack growth by grain boundary cavitation under cyclic loading. *Acta Mater.* **153**, 136–146 (2018).
- Williams, D. F., Cul, G. D. D., Toth, L. M. & Collins, E. D. The influence of Lewis acid/base chemistry on the removal of gallium by volatility from weapons-grade plutonium dissolved in molten chlorides. *Nucl. Technol.* **136**, 367–370 (2001).
- Li, H. et al. Corrosion and electrochemical investigations for stainless steels in molten Solar Salt: the influence of chloride impurity. *J. Energy Storage* **39**, 102675 (2021).
- D Souza, B., Zhuo, W., Yang, Q., Leong, A. & Zhang, J. Impurity driven corrosion behavior of HAYNES® 230® alloy in molten chloride salt. *Corros. Sci.* **187**, 109483 (2021).
- Doniger, W. H. et al. Investigation of impurity driven corrosion behavior in molten 2LiF-BeF₂ salt. *Corros. Sci.* **174**, 108823 (2020).
- Young, D. J. *High Temperature Oxidation and Corrosion of Metals*. (Elsevier, 2008).
- Liu, Y. et al. Corrosion of Cr in molten salts with different fluoroacidity in the presence of CrF₃. *Corros. Sci.* **169**, 108636 (2020).
- Ai, H. et al. Dissolved valence state of iron fluorides and their effect on Ni-based alloy in FLiNaK salt. *Corros. Sci.* **192**, 109794 (2021).
- Wu, B. et al. On the origin of tellurium corrosion resistance of hot-rolled GH3535 alloy. *Corros. Sci.* **170**, 108644 (2020).
- Cheng, H. et al. EPMA and TEM characterization of intergranular tellurium corrosion of Ni–16Mo–7Cr–4Fe superalloy. *Corros. Sci.* **97**, 1–6 (2015).
- Liu, Q. et al. Effect of graphite particles in molten LiF-NaF-KF eutectic salt on corrosion behaviour of GH3535 alloy. *Corros. Sci.* **168**, 108581 (2020).
- Chen, D. et al. Role of the grain-boundary phase on the elevated-temperature strength, toughness, fatigue and creep resistance of silicon carbide sintered with Al, B and C. *Acta Mater.* **48**, 4599–4608 (2000).
- Pataky, G. J., Sehitoğlu, H. & Maier, H. J. Creep deformation and mechanisms in Haynes 230 at 800 °C and 900 °C. *J. Nucl. Mater.* **443**, 484–490 (2013).
- Shrestha, S. L. et al. Creep resistance and material degradation of a candidate Ni–Mo–Cr corrosion resistant alloy. *Mater. Sci. Eng.* **674**, 64–75 (2016).
- Warhadpande, A., Sadeghi, F. & Evans, R. D. Microstructural alterations in bearing steels under rolling contact fatigue part 1-historical overview. *Tribol. T.* **56**, 349–358 (2013).
- Allen, T. R. et al. Materials challenges for generation IV nuclear energy systems. *Nucl. Technol.* **162**, 342–357 (2008).
- Xiao, Q. et al. Corrosion behavior of stainless steels in simulated PWR primary water: the effect of composition and matrix phases. *Corros. Sci.* **177**, 108991 (2020).
- Xu, Z., Jiang, L., Dong, J., Li, Z. & Zhou, X. The effect of silicon on precipitation and decomposition behaviors of M6C carbide in a Ni–Mo–Cr superalloy. *J. Alloy. Compd.* **620**, 197–203 (2015).

50. Olson, L. C., Ambrosek, J. W., Sridharan, K., Anderson, M. H. & Allen, T. R. Materials corrosion in molten LiF–NaF–KF salt. *J. Fluor. Chem.* **130**, 67–73 (2009).
51. Chen, T., Tiwari, G. N., Prasad, Iijima, Y. & Yamauchi, K. Volume and Grain Boundary Diffusion of Chromium in Ni-Base Ni-Cr-Fe Alloys. *Mater. Trans.* **44**, 40–46 (2003).
52. Weiss, I. & Jonas, J. J. Interaction between recrystallization and precipitation during the high temperature deformation of HSLA steels. *Metall. Trans. A* **10**, 831–840 (1979).
53. Iwashita, C. H. & Wei, R. P. Coarsening of grain boundary carbides in a nickel-based ternary alloy during creep. *Acta Mater.* **48**, 3145–3156 (2000).
54. Galvele, J. A stress corrosion cracking mechanism based on surface mobility. *Corros. Sci.* **27**, 1–33 (1987).
55. Danon, A. E. et al. Molten salt corrosion (FLiNaK) of a Ni–Mo–Cr alloy and its welds for application in energy-generation and energy-storage systems. *Corros. Sci.* **164**, 108306 (2020).
56. ASTM International. ASTM G39–99: Standard Practice for Preparation and Use of Bent-Beam Stress-Corrosion Test Specimens (2016).

ACKNOWLEDGEMENTS

We would like to thank the financial support from the Project of the National Natural Science Foundation of China [grant number 52075235], the Key R&D Program of Gansu Province [grant number 20YF3WA017], the Young Doctor Program of Education Department of Gansu Province [2022QB-050], and Key Research Program of Education Department of Gansu Province [GSSYLXM-03].

AUTHOR CONTRIBUTIONS

Y.G.: Conceptualisation, Methodology, Writing-Original draft preparation. W.Z.: Investigation, Data curation. Y.X.: Validation. Y.S.: Project administration, Supervision, Resources. K.V.: Supervision.

COMPETING INTERESTS

The authors declare no competing interests.

ADDITIONAL INFORMATION

Supplementary information The online version contains supplementary material available at <https://doi.org/10.1038/s41529-022-00300-x>.

Correspondence and requests for materials should be addressed to Youwei Xu or Yu Shi.

Reprints and permission information is available at <http://www.nature.com/reprints>

Publisher's note Springer Nature remains neutral with regard to jurisdictional claims in published maps and institutional affiliations.



Open Access This article is licensed under a Creative Commons Attribution 4.0 International License, which permits use, sharing, adaptation, distribution and reproduction in any medium or format, as long as you give appropriate credit to the original author(s) and the source, provide a link to the Creative Commons license, and indicate if changes were made. The images or other third party material in this article are included in the article's Creative Commons license, unless indicated otherwise in a credit line to the material. If material is not included in the article's Creative Commons license and your intended use is not permitted by statutory regulation or exceeds the permitted use, you will need to obtain permission directly from the copyright holder. To view a copy of this license, visit <http://creativecommons.org/licenses/by/4.0/>.

© The Author(s) 2022